GEOPHYSICS, VOL. 86, NO. 1 (JANUARY-FEBRUARY 2021); P. KS1–KS9, 13 FIGS., 1 TABLE.
10.1190/GEO2020-0084.1

Sparsity-promoting least-squares interferometric migration for high-resolution passive source location

Yujin Liu[1], Yue Du[1], and Yi Luo[2]

ABSTRACT

Seismic source localization plays an important role in estimating the hypocenter of earthquakes and in monitoring hydraulic fracturing. Interferometric crosscorrelation migration (ICCM) is one of the most important waveform-based source location methods that produces a source image from interstation crosscorrelations without manual picking. However, the ICCM method suffers from blurring of the source image, especially for cases in which the acquisition aperture is limited, receivers are sparsely distributed, and the data signal-to-noise ratio is too low. As a result, it typically cannot resolve sources in close proximity to each other, whereas distinguishing them might be a desired feature when we want to follow the fracture evolution in space and time. One possible solution is by fitting a source distribution function to the observed interstation crosscorrelations by least-squares minimization, where the source distribution function is a source power-spectral density (PSD) defined as a function of frequency and spatial location. However, this least-squares interferometric crosscorrelation migration (LS-ICCM) approach provides limited resolution improvement compared to the ICCM method. To further improve the image resolution, we have adopted a sparsity-promoting interferometric crosscorrelation migration (SP-ICCM) method that negates the effects of unfocused sources during the inversion. This sparsity constraint is imposed on the source PSD in space to mitigate the loss of resolution that arises as a consequence of incomplete information, including limited aperture and discretization. The inverse problem involving this sparsity constraint can be solved relatively quickly with an iteratively reweighted least-squares algorithm. Using synthetic and field data tests, we demonstrate that our method is robust to noise and effective for closely spaced sources in complex geologic settings.

INTRODUCTION

Seismic source location is of great importance for determining earthquake hypocenters in global seismology (Thurber and Engdahl, 2000) and monitoring hydraulic fractures in exploration seismology (Maxwell et al., 2010; Shapiro, 2015). Source locations are usually determined by picking the arrival times of seismic events and then searching for the minimum misfit between the theoretical and observed traveltimes by either an inversion algorithm or a grid search approach (Pujol, 2004). For example, the double-difference method estimates the source locations by minimizing the residuals between the theoretical and observed traveltime differences for pairs of earthquakes at each station while linking together all of the observed event-station pairs (Waldhauser and Ellsworth, 2000; Zhang and Thurber, 2003). For these traveltime-based methods, picking the arrival time is an inevitable step and only traveltime information is used for the source location. Traveltime picking is time-consuming, error-prone, and sometimes subjective, especially for complex events with a low signal-to-noise ratio (S/N). Missed arrival times and picking errors may directly cause location errors. In addition, most traveltime-based methods ignore the finite-frequency and multiple-scattering effects and cannot use the multichannel coherency of input data (Li et al., 2020).

To mitigate the limitations of traveltime-based methods, waveform-based source location methods without picking have been developed. One common waveform-based method is the partial waveform stacking (PWS) method. It involves stacking of the waveforms from individual receivers along theoretical traveltime

Manuscript received by the Editor 12 February 2020; revised manuscript received 21 August 2020; published ahead of production 4 October 2020; published online 04 January 2021.
[1]Aramco Beijing Research Center, Aramco Asia, Beijing 100102, China. E-mail: yujin.liu@aramcoasia.com (corresponding author); yue.du@aramcoasia.com.
[2]EXPEC Advanced Research Center, Saudi Aramco, Dhahran 31311, Saudi Arabia. E-mail: yi.luo@aramco.com.

DOI:10.1190/geo2020-0084.1

trajectories and over all possible initiation times. There are various alternatives to the PWS method that differ in preprocessing of the input waveforms. For example, Kao and Shan (2004) propose a source-scanning algorithm that identifies the seismic event location and origin time by stacking the absolute amplitudes of recorded data along theoretical traveltime trajectories. Another well-established waveform-based source location technique is time-reversal imaging (TRI). The principle of TRI is that the extrapolated wavefields from receivers focus at the initial position of the seismic sources given a reasonably accurate velocity model (McMechan, 1982; Gajewski and Tessmer, 2005; Fink, 2006). Because this approach is similar to reverse time migration (RTM) in exploration seismology, the imaging conditions proposed for RTM can be adapted to TRI for the source location. Among various types of imaging conditions, the most straightforward one is scanning the full 4D (1D in time and 3D in space) wavefield and then searching the locations with the strongest amplitude. Douma et al. (2013) improve the temporal and spatial resolutions of the TRI method using deconvolution during wavefield back propagation. Inspired by the crosscorrelation imaging condition used in RTM, Artman et al. (2010) propose a zero-lag autocorrelation imaging condition for source localization using P-P and S-S waves and a zero-lag crosscorrelation imaging condition for source localization using P-S waves. Yang and Zhu (2019) further introduce an elastic source image technique that is based on P- and S-wave separation and demonstrate that it can be used for characterizing complex earthquake dynamic ruptures. As explored in active seismic scenarios (Rickett and Sava, 2002; Sava and Fomel, 2006), wavefield correlation beyond zero-lag generates so-called extended images (Witten and Shragge, 2015; Rocha et al., 2019), which could be used to update velocity models (Shabelansky et al., 2015; Witten and Shragge, 2017a, 2017b). However, as pointed out by Nakata and Beroza (2016), stacking all of the receiver wavefields at each space and time sample before correlation can be considered as an arithmetic-mean imaging condition, which produces low-resolution source images with artifacts when the number of receivers is insufficient. Sun et al. (2015) and Nakata and Beroza (2016) independently propose a geometric-mean imaging condition to improve the spatial resolution of the source image. This imaging condition multiplies all of the receiver wavefields at each space and time sample, and it requires wavefields propagation using data from each receiver separately. This leads to a huge computational cost for the wave-equation implementation. To reduce the computational burden, Sun et al. (2015) propose a hybrid multiplicative TRI method that multiplies wavefields back propagated from groups of receivers and then applies a causal integration over time to obtain the source evolution process. Zhu et al. (2019) further demonstrate that the hybrid multiplicative imaging condition performs better than the crosscorrelation imaging condition in the presence of strong noise. However, Sun et al. (2016) show that the time-reversal wavefield may not reconstruct the amplitude and phase information of the source functions. This problem can be addressed by full-waveform inversion (FWI). In fact, FWI has already been used to solve for event location and source mechanism for more than two decades (e.g., Wu and McMechan, 1996). Recent studies are trying to improve the spatial resolution of the source image by adding a sparsity-promoting term in the objective function (Gao et al., 2017; Sharan et al., 2018; Li et al., 2019).

Another choice of a waveform-based source localization method without traveltime picking is interferometric crosscorrelation migration (ICCM), which uses interstation crosscorrelograms to determine the source distribution (Schuster et al., 2004). For passive seismic data stimulated by a continuous source signature, such as the source generated by the drill bit when it fractures the surrounding rocks, the crosscorrelation of traces can collapse the ring-like source wavelet into an impulse-like wavelet, leading to good spatial resolution compared to the original TRI method. Moreover, the ICCM method does not need to know the excitation source time because the interstation crosscorrelation cancels the common traveltime (including the excitation time) recorded by these two stations. However, it provides a source image with limited spatial resolution. One reason is that the frequency spectra of the source wavelets have been squared after crosscorrelation. To eliminate the wavelet effect, Wu et al. (2017) introduce a deconvolution migration method by combining deconvolution interferometry with interferometric crosscorrelation migration. However, as Schuster et al. (2004) point out, the spatial resolution of the source image is poor mainly because the vertical wavenumber of the image provided by the ICCM method is inherently small, especially for limited apertures and sparse sampling acquisition. This problem might be mitigated using the emergent angle estimated from the crosscorrelograms as a constraint during migration. However, it is challenging to measure this emergent angle when the sensors are sparsely distributed. Similar to the study of solar structure and dynamics in helioseismology (Woodard, 1997; Gizon and Birch, 2002; Hanasoge et al., 2011), Tromp et al. (2010) propose a noise crosscorrelation tomography method to update the model parameters by minimizing a measure of the difference between observed and simulated ensemble crosscorrelations. Rather than updating the model parameters, there are numerous investigations in constructing sensitivity kernels of ensemble crosscorrelation measurements to locate seismic sources (Basini et al., 2013; Hanasoge, 2013, 2014; Fichtner, 2014; Ermert et al., 2016). However, most of these studies focus on the effects of noisy source distributions on ambient noise tomography; little attention has been paid to address the issue related to the lack of spatial resolution in the crosscorrelation imaging of seismic sources.

In this paper, we present a sparsity-promoting crosscorrelation waveform inversion method to improve the spatial resolution of the source image. Sparseness in the source distribution function is a valid and useful criterion for supplying the missing information, including limited aperture and discretization. This is equivalent to assuming a smooth amplitude variation in the transition between known and unknown (missing) data. We first review the forward problem that describes how the source power-spectral density (PSD) distribution maps into the interstation crosscorrelations. Then, we introduce least-squares and sparsity-promoting solutions to invert this forward map. Using synthetic and field data experiments, we demonstrate the effectiveness of our proposed sparsity-promoting method for situations of increasing complexity including noise and realistic geology.

THEORY

In this section, we first review the forward problem that simulates interstation crosscorrelograms from the source PSD. Then, we derive a ray-based simplification of the forward operator and demonstrate that the ICCM method proposed by Schuster et al. (2004) is its adjoint operator. Finally, we present two waveform inversion methods to estimate the source PSD from the observed crosscorrelograms. The first one is least-squares interferometric crosscorrelation migration (LS-ICCM) as proposed by Basini et al. (2013),

DOI:10.1190/geo2020-0084.1

Hanasoge (2013, 2014), Fichtner (2014), and Ermert et al. (2016); the second one is the sparsity-promoting interferometric crosscorrelation migration (SP-ICCM) proposed in this paper.

Forward problem

A seismic wavefield $u(\mathbf{x}_{r_i},\omega)$ at the receiver position $\mathbf{x}_{r_i}$ is connected with sources at $\mathbf{x}_{s_n}$ by the representation theorem (Aki & Richards, 2002):

$$u(\mathbf{x}_{r_i},\omega)=\sum_{n=1}^{N_s}S(\mathbf{x}_{s_n},\omega)G(\mathbf{x}_{r_i},\mathbf{x}_{s_n},\omega), \tag{1}$$

where ω is the angular frequency, N_s is the total number of sources, $S(\mathbf{x}_{s_n},\omega)$ is the frequency spectrum of a source at $\mathbf{x}_{s_n}$, and $G(\mathbf{x}_{r_i},\mathbf{x}_{s_n},\omega)$ is the Green's function. The crosscorrelation between the seismic wavefield at $\mathbf{x}_{r_i}$ and $\mathbf{x}_{r_j}$ can be expressed as

$$\begin{aligned}\mathcal{C}(\mathbf{x}_{r_i},\mathbf{x}_{r_j},\omega)&=u^*(\mathbf{x}_{r_i},\omega)u(\mathbf{x}_{r_j},\omega)\\&=\sum_{m=1}^{N_s}\sum_{n=1}^{N_s}S^*(\mathbf{x}_{s_m},\omega)G^*(\mathbf{x}_{r_i},\mathbf{x}_{s_m},\omega)S(\mathbf{x}_{s_n},\omega)G(\mathbf{x}_{r_j},\mathbf{x}_{s_n},\omega),\end{aligned} \tag{2}$$

where $u^*(\mathbf{x}_{r_i},\omega)$ is the complex conjugate of $u(\mathbf{x}_{r_i},\omega)$. Due to the transient nature of seismic sources, $\mathcal{C}(\mathbf{x}_{r_i},\mathbf{x}_{r_j},\omega)$ is generally different when using different time intervals. We therefore consider the expectation

$$\begin{aligned}E[\mathcal{C}(\mathbf{x}_{r_i},\mathbf{x}_{r_j},\omega)]&=C(\mathbf{x}_{r_i},\mathbf{x}_{r_j},\omega)\\&=\sum_{m=1}^{N_s}\sum_{n=1}^{N_s}G^*(\mathbf{x}_{r_i},\mathbf{x}_{s_m},\omega)G(\mathbf{x}_{r_j},\mathbf{x}_{s_n},\omega)E[S^*(\mathbf{x}_{s_m},\omega)S(\mathbf{x}_{s_n},\omega)],\end{aligned} \tag{3}$$

that can be approximated by the stack over many time intervals (for instance 1 h windows throughout a day). In equation 3, the term $E[S^*(\mathbf{x}_{s_m},\omega)S(\mathbf{x}_{s_n},\omega)]$ denotes the expected correlation of sources at position $\mathbf{x}_{s_m}$ and $\mathbf{x}_{s_n}$. The evaluation of equation 3 is prohibitively expensive, not only due to the double summation, but also because many simulations are required for multiple sources. Thus, equation 3 is only used for simplified wave propagation scenarios (Cupillard and Capdeville, 2010; van Driel et al., 2015; Fichtner et al., 2017).

To reduce computational costs, we assume that the correlation between different noise sources decays relatively quickly with distance compared to the seismic wavelength and that the contribution from colocated noise sources to the correlation function is dominant. We therefore make the approximation

$$E[S^*(\mathbf{x}_{s_m},\omega)S(\mathbf{x}_{s_n},\omega)]=I(\mathbf{x}_{s_n},\omega)\delta(\mathbf{x}_{s_m}-\mathbf{x}_{s_n}), \tag{4}$$

where $I(\mathbf{x}_{s_n},\omega)$ is the PSD of passive sources at $\mathbf{x}_{s_n}$. This is a frequently used assumption (Woodard, 1997; Tromp et al., 2010; Hanasoge, 2013, 2014; Fichtner, 2014; Nishida, 2014), and its accuracy has to be assessed for each data set. For uncorrelated noise sources, equation 3 simplifies to

$$C(\mathbf{x}_{r_i},\mathbf{x}_{r_j},\omega)=\sum_{n=1}^{N_s}G^*(\mathbf{x}_{r_i},\mathbf{x}_{s_n},\omega)G(\mathbf{x}_{r_j},\mathbf{x}_{s_n},\omega)I(\mathbf{x}_{s_n},\omega). \tag{5}$$

Compared to equation 3, the double summation reduces to a single summation in equation 5, thus facilitating the forward computation of the noise correlation functions.

Interferometric crosscorrelation migration

To further simplify the forward mapping described in equation 5, we consider the far-field Green's function under the high-frequency approximation:

$$G(\mathbf{x}_{r_i},\mathbf{x}_{s_n},\omega)=A(\mathbf{x}_{r_i},\mathbf{x}_{s_n})e^{-i\omega t(\mathbf{x}_{r_i},\mathbf{x}_{s_n})}, \tag{6}$$

where $t(\mathbf{x}_{r_i},\mathbf{x}_{s_n})$ and $A(\mathbf{x}_{r_i},\mathbf{x}_{s_n})$ are the traveltimes and amplitudes, respectively, from the source at $\mathbf{x}_{s_n}$ to the receiver at $\mathbf{x}_{r_i}$. Because the source localization is mainly dependent on the kinematic information embedded in the traveltime term, the amplitude term is ignored in the following equations. Here the traveltime is calculated by the second-order fast-marching method (Rickett and Fomel, 1999).

Substituting the Green's function in equation 6 into equation 5 for the forward modeling produces

$$C(\mathbf{x}_{r_i},\mathbf{x}_{r_j},\omega)=\sum_{n=1}^{N_s}I(\mathbf{x}_{s_n},\omega)e^{-i\omega[t(\mathbf{x}_{r_j},\mathbf{x}_{s_n})-t(\mathbf{x}_{r_i},\mathbf{x}_{s_n})]}, \tag{7}$$

where $t(\mathbf{x}_{r_j},\mathbf{x}_{s_n})$ are the traveltimes from source at $\mathbf{x}_{s_n}$ to receiver at $\mathbf{x}_{r_j}$. The adjoint formulation of equation 7 is

$$I(\mathbf{x}_{s_n},\omega)=\sum_{j=1}^{N_r}\sum_{i=0}^{N_r}C(\mathbf{x}_{r_i},\mathbf{x}_{r_j},\omega)e^{i\omega[t(\mathbf{x}_{r_j},\mathbf{x}_{s_n})-t(\mathbf{x}_{r_i},\mathbf{x}_{s_n})]}, \tag{8}$$

where N_r is the total number of receivers. After summation of all frequency components of $I(\mathbf{x}_{s_n},\omega)$, we obtain the formula of ICCM for source localization (Schuster et al., 2004). Therefore, we demonstrate that the ICCM could be regarded as the adjoint of the interferometric crosscorrelation modeling.

To better understand the physical meaning of the forward modeling (equation 7) and its adjoint (equation 8), we use cartoons to illustrate them. Figure 1a shows the wave propagation generated by a seismic source at s_n. Two receivers r_i and r_j are placed at the surface to record the stimulated wavefield. Considering the receivers r_i as a virtual source, the crosscorrelogram data computed at r_j can be simulated by back propagating a source function at r_i, scattering at s_n, and then forward propagating to r_j, as shown in Figure 1b. The adjoint procedure back propagates the source function and the crosscorrelogram data, and then applies a zero-lag crosscorrelation imaging condition to the back-propagated wavefields, as shown in Figure 1c.

Least-squares interferometric crosscorrelation migration

Equation 7 provides a forward mapping for the calculation of interstation crosscorrelograms that can be compared with the observed crosscorrelograms. The forward mapping at each frequency can be rewritten into a matrix form as

$$\mathbf{d}=\mathbf{L}\mathbf{m}, \tag{9}$$

where $\mathbf{d}$ is a vector of interstation crosscorrelograms, $\mathbf{m}$ is a vector of source PSDs, and $\mathbf{L}$ is the forward operator that maps the source PSDs into interstation crosscorrelograms.

The optimal estimation of source PSDs can be achieved by minimizing the objective function

$$J(\mathbf{m}) = \frac{1}{2}\|\mathbf{W}_d(\mathbf{Lm} - \mathbf{d}_{obs})\|_p^p + \frac{\lambda}{2}\|\mathbf{W}_m\mathbf{m}\|_q^q, \quad (10)$$

where the first term measures the interstation crosscorrelogram misfit (or data misfit), the second term imposes model regularization, λ is a trade-off parameter between these two terms, $\mathbf{W}_d$ is a matrix of data weights (which is often a diagonal matrix containing the inverse of the standard deviation of the data), and $\mathbf{W}_m$ is a matrix of model weights that can enhance features of the model, for example, resolution or smoothness. In equation 10, p and q indicate different norms that can be applied to measure the norm of vectors. When $p = q = 2$ and $\mathbf{W}_m$ is an identity matrix, the solution of equation 10 can be expressed explicitly as

$$\mathbf{m} = (\mathbf{L}^T\mathbf{W}_d^T\mathbf{W}_d\mathbf{L} + \lambda\mathbf{I})^{-1}\mathbf{L}^T\mathbf{W}_d^T\mathbf{W}_d\mathbf{d}_{obs}. \quad (11)$$

This is a damped least-squares solution; the inverse of the matrix in parentheses can be solved accurately by matrix decomposition methods or approximately by iterative methods. In this paper, we use a diagonal pivoting method with a partial pivoting strategy (Bunch and Kaufman, 1977). As pointed out by Claerbout (1992), iterative methods, such as the conjugate gradient method, should be used to solve large-scale inverse problems for high efficiency. The damped least-squares solution of equation 11 is similar to the cross-correlation imaging method proposed by Basini et al. (2013), Hanasoge (2013, 2014), Fichtner (2014), and Ermert et al. (2016). Here, we refer to the damped least-squares solution as LS-ICCM.

Sparsity-promoting interferometric crosscorrelation migration

A sparse model can be obtained by choosing a norm that does not penalize large elements contained in the model. One common approach is to choose an L_1 norm for the model and an L_2 norm for the data misfit in equation 10. The mixed-norm problem can be solved by a variety of sparsity-promoting solvers such as the fast iterative shrinkage thresholding (Beck and Teboulle, 2009) and linearized Bregman (Yin et al., 2008). A discussion of the merits of these solvers is beyond the scope of this paper. One of the most popular approaches is by transforming the mixed-norm problem into an $L_2 - L_2$ problem by using a model-dependent weighting matrix $\mathbf{W}_m$, where the ith diagonal element of $\mathbf{W}_m$ is chosen to be a function of the ith component of the model vector $\mathbf{m}$ as follows:

$$\mathrm{diag}(\mathbf{W}_m)_i = \frac{1}{\sqrt{|m_i| + \varepsilon}}, \quad (12)$$

where ε is a threshold chosen to avoid division by zero. This threshold is set to be a percentage of the maximum value in the model vector. The smaller the percentage, the sparser the solution. Hence, this number defines a second trade-off between sparseness and smoothness. The same percentage can be used for all frequencies.

The model that minimizes the objective function in equation 10 can be expressed as

$$\mathbf{m} = (\mathbf{L}^T\mathbf{W}_d^T\mathbf{W}_d\mathbf{L} + \lambda\mathbf{W}_m^T\mathbf{W}_m)^{-1}\mathbf{L}^T\mathbf{W}_d^T\mathbf{W}_d\mathbf{d}_{obs}. \quad (13)$$

Because $\mathbf{W}_m$ depends on the model, solving equation 13 is a nonlinear inverse problem. To invert the matrix in equation 13, the iteratively reweighted least-squares (IRLS) algorithm (Scales et al, 1988) is used due to its simplicity and efficiency. In the IRLS method, the nonlinear inverse problem is solved iteratively by fixing the weighting matrix $\mathbf{W}_m$ and then inverting the matrix $\mathbf{L}^T\mathbf{W}_d^T\mathbf{W}_d\mathbf{L} + \lambda\mathbf{W}_m^T\mathbf{W}_m$ within each iteration. Also, the weighting matrix $\mathbf{W}_m$ is updated iteratively using the previous solution of the linear problem. Similar to LS-ICCM, the linear inverse problem within each iteration is solved by the diagonal pivoting method with the partial pivoting strategy. Here, we refer to this sparsity-promoting solution as SP-ICCM. This method is summarized in Algorithm 1, where $f(\mathbf{m})$ describes equation 12 and the "condition" represents a convergence check (for example, tolerance of the residual and maximum number of iterations).

Algorithm 1. IRLS method for SP-ICCM.

$\mathrm{m} \Leftarrow \left(\mathbf{L}^T\mathbf{W}_d^T\mathbf{W}_d\mathbf{L} + \lambda\mathbf{I}\right)^{-1}\mathbf{L}^T\mathbf{W}_d^T\mathbf{d}_{obs}$
while condition **do**
  $\mathbf{W}_m \Leftarrow \mathrm{f}(\mathbf{m})$
  $\mathrm{m} \Leftarrow \left(\mathbf{L}^T\mathbf{W}_d^T\mathbf{W}_d\mathbf{L} + \lambda\mathbf{W}_m^T\mathbf{W}_m\right)^{-1}\mathbf{L}^T\mathbf{W}_d^T\mathbf{d}_{obs}$
end while

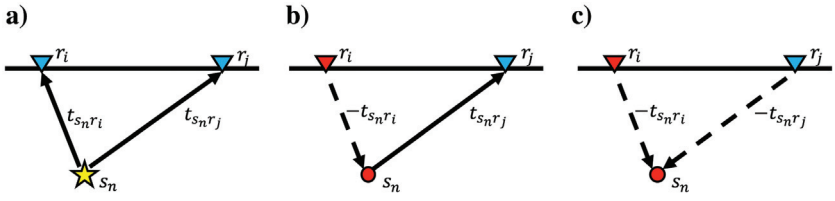

Figure 1. Schematic illustrations of the (a) observation, (b) forward modeling, and (c) interferometric migration. The solid arrows show the direction of forward propagation, and the dashed arrows show the direction of back propagation.

RESULTS

In this section, we use synthetic and field data to demonstrate the resolution improvement of the SP-ICCM method over the ICCM and LS-ICCM methods. In the synthetic data tests, single- and multi-source cases are considered. Moreover, random noise is added to the synthetic data to test the noise robustness of the SP-ICCM method. Finally, the field data are used to demonstrate the effectiveness of the SP-ICCM method.

Synthetic data tests

Here, a 2D acoustic finite-difference modeling method is used to generate synthetic data. We use a small section of the Marmousi II model (Martin et al., 2002) to introduce some complexity into the numerical experiments (Figure 2a). In this section, we have 11.2 km $< x <$ 13.4 km and 5.1 km $< z <$ 7.7 km. A seismic source located

at $x_s = 2.0$ km and $z_s = 1.5$ km, shown with a yellow cross in Figure 2a, is just below the high-velocity layer. The source-time function is a Ricker wavelet with a peak frequency of 20 Hz. Twenty receivers at every 200 m are placed at the surface. Figure 2b shows the synthetic seismic data without noise. Using this type of sensor network with sparse sampling and limited coverage, the spatial resolution of a source image is often poor due to the incomplete interference of the wave components (Sava, 2011). Furthermore, to demonstrate the noise robustness of the proposed methods, we add strong random noise to the synthetic data, as shown in Figure 2c. The S/N of the noisy data is −7.4 dB. Here, S/N is defined as $10\log_{10} E_{\text{signal}}/E_{\text{noise}}$, where E_{signal} and E_{noise} are the stacking powers of the signal and noise, respectively.

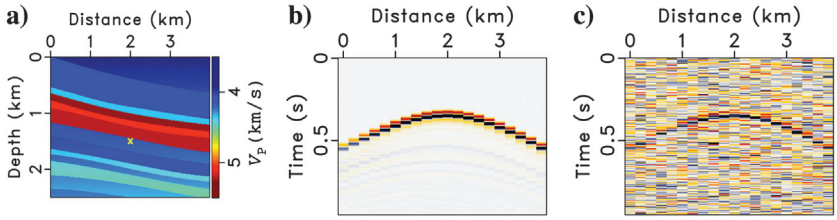

Figure 2. (a) Acoustic velocity model (a part of the Marmousi II model). The yellow cross indicates the source location. The receivers are deployed on the surface. (b) Synthetic data without noise and (c) synthetic data with random noise added (S/N = −7.4 dB).

As mentioned previously, the input data of the ICCM, LS-ICCM, and SP-ICCM methods are the crosscorrelograms generated by computing the interstation crosscorrelations. Assuming that there are N_r receivers, then the total number of crosscorrelograms should be $N_r \times (N_r - 1)/2$. In this case, the total number of crosscorrelograms is 190. Figure 3a and 3b shows the crosscorrelograms using noise-free and noisy data, respectively. Although the stacking operation in the crosscorrelation can suppress a certain amount of random noise, there is still strong noise present after crosscorrelation.

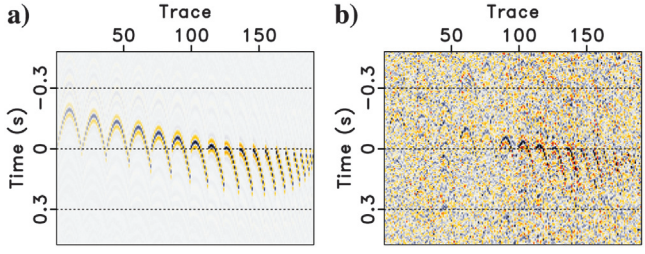

Figure 3. Crosscorrelograms using the (a) noise-free data and (b) noisy data.

Using the noise-free data, we first compare the source images provided by the ICCM, LS-ICCM, and SP-ICCM methods with and without velocity errors, as shown in Figure 4. It is evident that, regardless of the velocity accuracy, the SP-ICCM image has much higher resolution than either the ICCM or LS-ICCM images, and that the LS-ICCM image has slightly higher resolution than that of the ICCM method. It is worth noting that, although the source images move downward when the velocity is too slow and upward when the velocity is too fast, all source images focus very well. This indicates that the in-

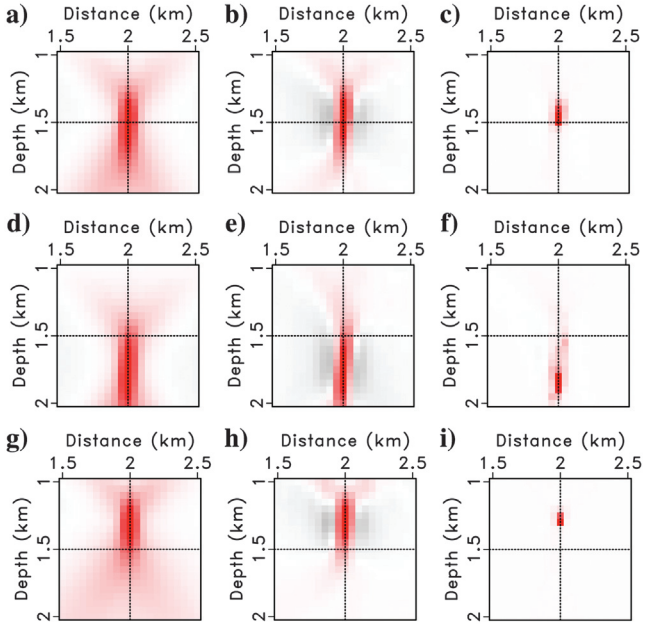

Figure 4. Source images of the ICCM, LS-ICCM and SP-ICCM methods using (a–c) the correct velocity, (d–f) 10% slower velocity, and (g–i) 10% faster velocity. The left, middle, and right columns show the ICCM, LS-ICCM, and SP-ICCM images, respectively. The intersection of the black dotted lines indicates the true source location.

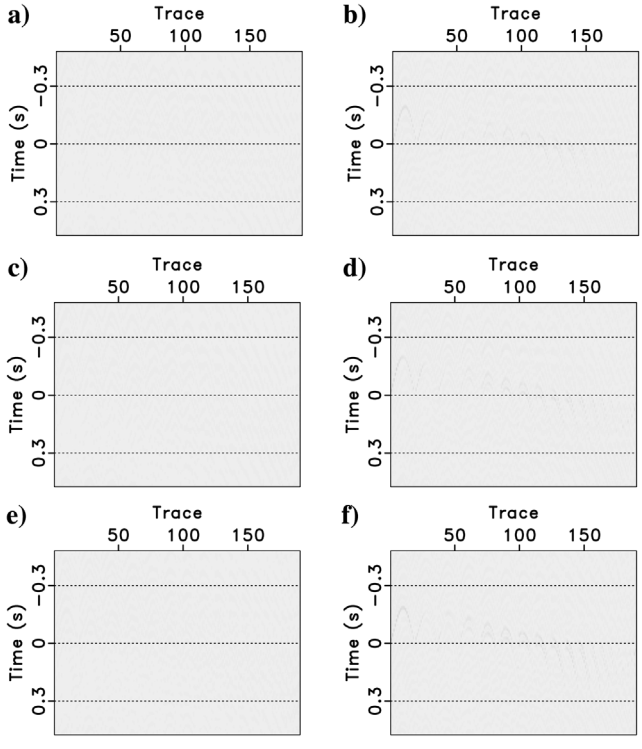

Figure 5. Data residuals of the LS-ICCM and SP-ICCM methods using (a–b) the correct velocity, (c–d) 10% slower velocity, and (e–f) 10% faster velocity. The left and right columns show the LS-ICCM and SP-ICCM crosscorrelogram residuals, respectively.

verted source PSD is capable of generating crosscorrelograms that fit the observed ones even when the velocity is inaccurate. Therefore, there is no cycle-skipping issue in the inversion-based source imaging method. This can be verified by computing the crosscorrelogram residuals after inversion, as shown in Figure 5. It shows that the LS-ICCM method generates negligibly small residuals after inversion and that the SP-ICCM has slightly larger, but still very small residuals due to the effects of the sparsity-promoting regularization term. Thus, we demonstrate that the inversion-based source imaging methods do not have a cycle-skipping problem.

Then, we test the robustness of the SP-ICCM method in the presence of strong band-limited random noise. Figure 3b shows the input crosscorrelograms, which are generated by the noisy data in Figure 2c. Figure 6 shows the source images generated by the ICCM, LS-ICCM, and SP-ICCM methods with correct, 10% slower, and 10% faster velocities. It is apparent that the spatial resolution of the ICCM image is slightly improved by the LS-ICCM method and that the SP-ICCM method provides remarkably clear high-resolution images compared with the ICCM and LS-ICCM methods. Similar to the noise-free case, the data residuals from the LS-ICCM and SP-ICCM methods are negligible whether the velocity is correct or not, as shown in Figure 7.

Finally, we perform a multisource location experiment on the same Marmousi II model. The acquisition system retains the same parameters as in the first single-source example. The only difference is that there are three sources located under the high-velocity layer, as denoted by the yellow crosses in Figure 8a. They are evenly distributed from $x = 1.8$ km to $x = 2.2$ km with a spacing of 258 m. These sources from left to right act at $t = 0.05$ s, $t = 0.1$ s, and $t = 0.2$ s, respectively. Their source functions are Ricker wavelets with the same amplitude and frequency range. Because the average velocity above the sources is approximately 5 km/s and the peak frequency of the wavelets is 20 Hz, the estimated wavelength is approximately 250 m, which is similar to the source spacing. Figure 8b shows the acoustic finite-difference modeling data. To make the multisource test more realistic, strong random noise is added to the synthetic data, as shown in Figure 8c. The S/N of the noisy data is −7 dB.

Following the same procedure as the one used in the single-source location experiment, we first generate crosscorrelograms from the observed data, and then we invert the source PSDs by minimizing the misfit between the synthetic and observed crosscorrelograms. Figure 9 shows the source images produced by the ICCM, LS-ICCM, and SP-ICCM methods with the correct, 10% slower, and 10% faster velocities. From these results, we can see that all of these methods successfully detect multiple source simultaneously even in the presence of strong noise. Compared with the ICCM and LS-ICCM images, the SP-ICCM image has the highest spatial resolution and S/N. We further calculate the crosscorrelogram residuals of the LS-ICCM and SP-ICCM methods, as shown in Figure 10. Similar to previous experiments, the LS-ICCM and SP-ICCM methods provide negligible residuals regardless of the velocity errors.

Field data tests

In this section, we demonstrate the effectiveness of the LS-ICCM and SP-ICCM methods with field data recorded on a 2D geophone array. This array is part of a 3D acquisition system specially designed for a seismic-while-drilling (SWD) trial test in the Middle East. In this SWD test, seismic signals generated by the drill bit are

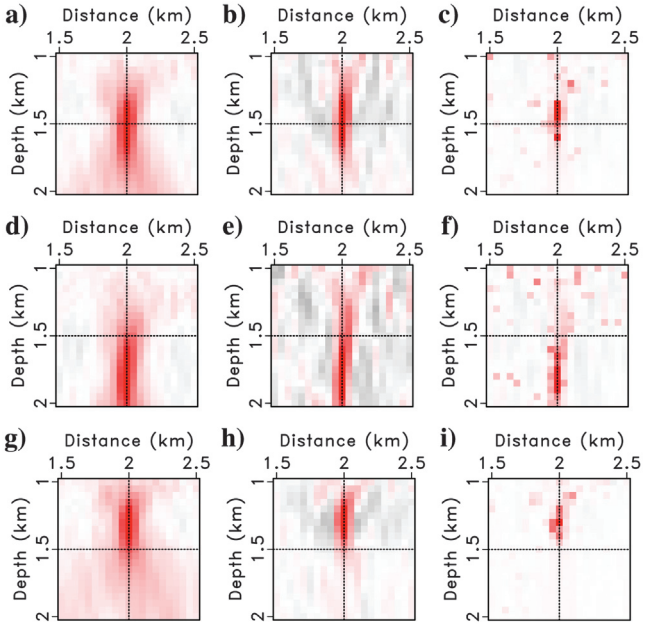

Figure 6. Noise-robustness comparisons of the ICCM, LS-ICCM, and SP-ICCM methods using (a–c) the correct velocity, (d–f) 10% slower velocity, and (g–i) 10% faster velocity. The left, middle, and right columns show the ICCM, LS-ICCM, and SP-ICCM images, respectively. The intersection of the black dotted lines indicates the true source location.

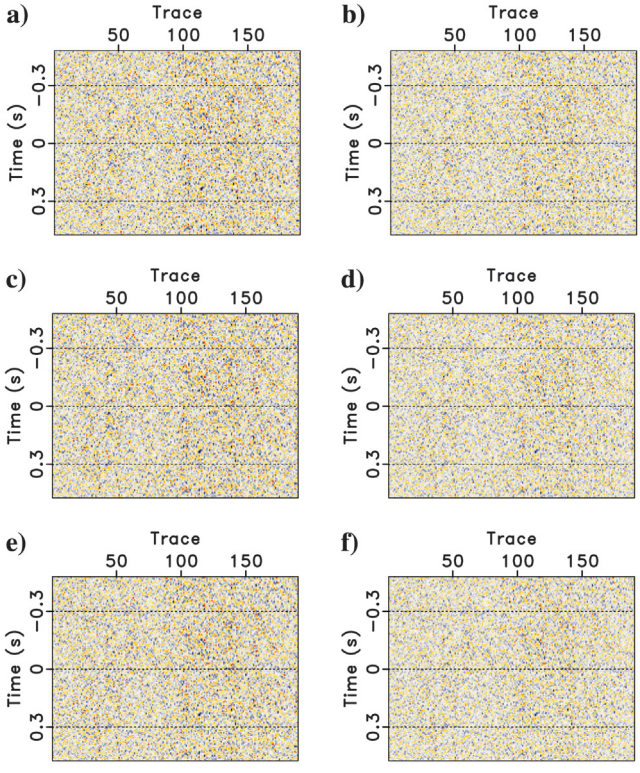

Figure 7. Data residuals of the LS-ICCM and SP-ICCM methods using (a–b) the correct velocity, (c–d) 10% slower velocity, and (e–f) 10% faster velocity. The left and right columns show the LS-ICCM and SP-ICCM data residuals, respectively.

DOI:10.1190/geo2020-0084.1

recorded passively by the seismic sensors on the surface while drilling (Rector and Marion, 1991; Poletto and Miranda, 2004).

Figure 11a shows the 1D velocity model used for source imaging. The model is estimated from a VSP survey. Figure 11b shows the preprocessed shot gather, which is generated from 1 h long continuous recordings. The preprocessing steps involve (a) producing a pilot trace with a time-delay correlation, (b) deconvolving the geophone data with the pilot trace, (c) 3D-to-2D conversion by multiplying the data spectra by $\sqrt{i/\omega}$, and (d) gaining the resulting data by $\sqrt{t}$ (Barton, 1989). In this survey, the offset ranges from −1.6 to 1.6 km and the receiver spacing interval is 25 m. The minimum offset is 75 m. The direct wave is very weak, as shown by the red arrows in Figure 11b. Because only the direct wave is needed to estimate the source location, we extract it from the preprocessed data using a 0.1 s window. Additionally, a velocity-model-based diffraction (Moser et al., 1999) filter is applied to the windowed data to improve the event continuity. The extracted direct wave is shown in Figure 11c.

Then, we use the preprocessed data to generate crosscorrelograms and locate the drill bit. Figure 12 shows the source images computed by the ICCM, LS-ICCM, and SP-ICCM methods. Comparing these three images shows that the SP-ICCM migration produces the source image with the cleanest location of the drill bit. Specifically, the SP-ICCM image has the highest spatial resolution and is the least contaminated by noise. However, we can observe in Figure 12 that the source location indicated by the SP-ICCM method is shallower than the true drill bit location, which might be caused by velocity errors. Now, notice that the other two methods cannot provide unambiguous source locations because of the blurring effect caused by the limited acquisition and noise in the data. We then compute the data residuals of LS-ICCM and SP-ICCM methods. The LS-ICCM and SP-ICCM residuals of coherent events are relatively small compared with the input crosscorrelograms, as indicated by the red arrows in Figure 13.

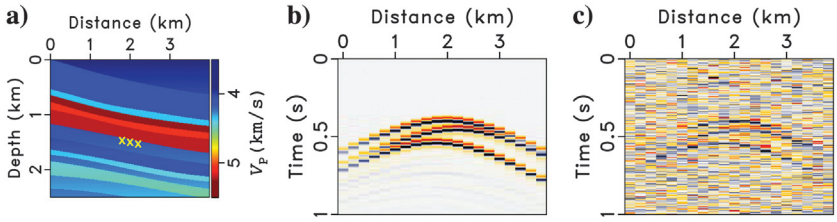

Figure 8. (a) The yellow crosses on the velocity model indicate the true locations of the multisource. The receivers are deployed on the surface. (b) Synthetic data without noise and (c) synthetic data with random noise added (S/N = −7 dB).

DISCUSSION

Although the forward and inverse problems in this paper are formulated in the acoustic medium, it is straightforward to extend them to an elastic medium. Two alternative approaches can be taken in this scenario where modifications are applied to the input crosscorrelograms and the forward/adjoint operators. The first one decomposes multicomponent data into P- and S-components, takes the P-P, S-S, and P-S correlations as input, and then constructs the forward and adjoint operators under

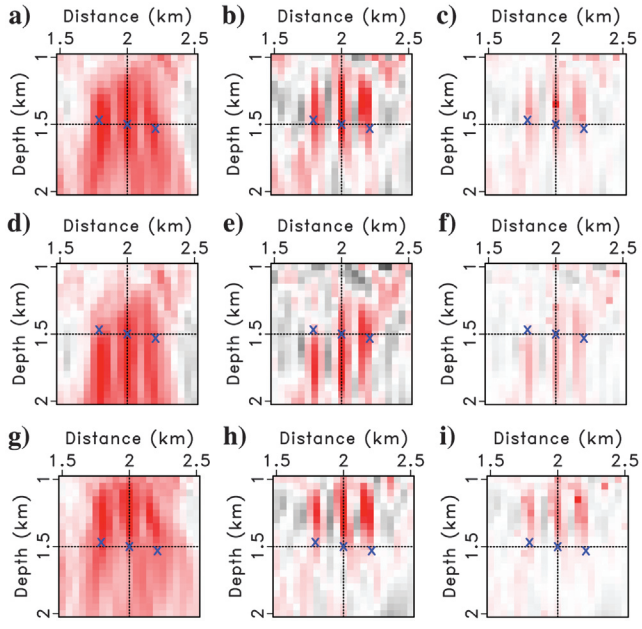

Figure 9. Multisource images produced by the ICCM, LS-ICCM, and SP-ICCM methods using (a–c) the correct velocity, (d–f) 10% slower velocity, and (g–i) 10% faster velocity. The left, middle, and right columns show the ICCM, LS-ICCM, and SP-ICCM images, respectively. The blue crosses indicate the true source locations.

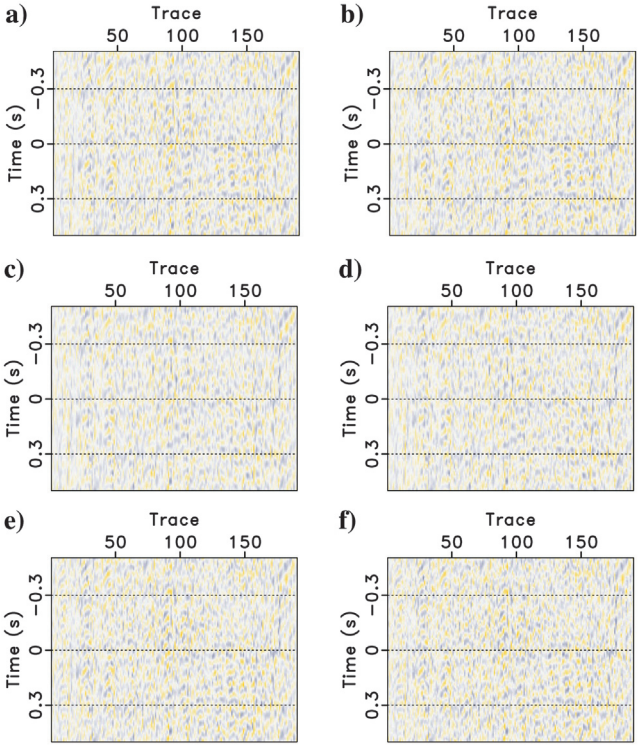

Figure 10. Data residuals of the LS-ICCM and SP-ICCM methods using (a–b) the correct velocity, (c–d) 10% slower velocity, and (e–f) 10% faster velocity. The left and right columns show the LS-ICCM and SP-ICCM data residuals, respectively.

the acoustic approximation. The second approach takes the single- and mixed-component correlations directly as inputs and then constructs the forward and adjoint operators by solving an elastic wave equation. A comparison of these two approaches is beyond the scope of this paper. However, it is worth noting that each of these two approaches could generate multiple source images and that the consistency of these images could be incorporated into the objective function to update the velocity models (Witten and Shragge, 2017a, 2017b).

Now, for the acoustic source imaging studied in this paper, the inverted source PSDs can achieve small crosscorrelogram misfits regardless of the velocity accuracy. This indicates that, without prior information about the source location, it is challenging to decouple the velocity model from the source location by only minimizing the scalar-wave crosscorrelogram waveform misfit. To invert both the source locations and velocity models through scalar-wave data, it might be necessary to design a new objective function (Ermert et al., 2016) and use second-order optimization algorithms (Sager et al., 2018). This subject should be investigated in the future.

It is worth noting that, for multisource imaging, the proposed method requires that the correlation between different sources decays relatively quickly with distance compared to the seismic wavelength. When this assumption is violated, noncolocated sources will generate nonnegligible crosstalk in the final source image. This crosstalk might be suppressed by careful data preprocessing such as data selection and dip filtering (Moser et al., 1999). More work is ongoing to eliminate this crosstalk during the inversion (Cupillard and Capdeville, 2010; van Driel et al., 2015; Fichtner et al., 2017).

We have demonstrated that, by imposing sparsity constraints on the source locations, the SP-ICCM method shows robustness in the presence of strong band-limited random noise. However, it will be affected by strong coherent noise that cannot be properly simulated by the forward modeling operator. Thus, it would be necessary to suppress the coherent noise before performing this sparsity-promoting waveform inversion method. In the field data tests used in this paper, we extract a small window around the direct wave to reduce the effects of coherent noise.

This paper presents a general inversion framework to estimate the source PSD from interstation crosscorrelograms. It is easy to incorporate other prior information about the source distribution, other sparsity promoting solvers, and other types of norms to measure the misfit. In addition, although Kirchhoff-type modeling and migration operators are used in this paper to validate the SP-ICCM method, it is straightforward to adapt it to wave-equation-based operators within the same inversion framework.

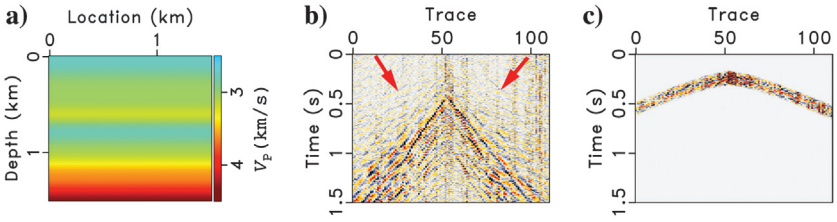

Figure 11. (a) Velocity model, (b) preprocessed data, and (c) extracted window around the direct arrival.

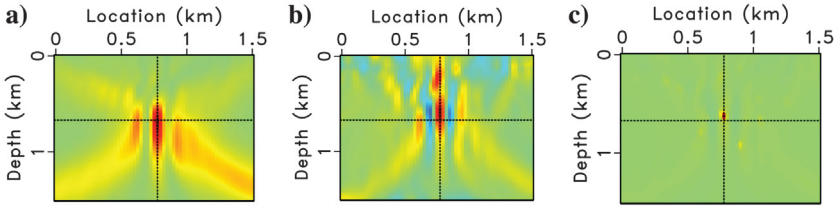

Figure 12. Source images produced by the (a) ICCM, (b) LS-ICCM, and (c) SP-ICCM methods. The intersection of the black dotted lines indicates the true source location.

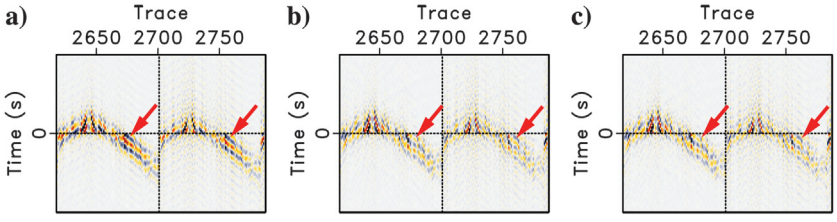

Figure 13. Crosscorrelogram comparison: (a) input crosscorrelograms, (b) crosscorrelogram residuals of the LS-ICCM method, and (c) crosscorrelogram residuals of the SP-ICCM method.

CONCLUSION

We propose a sparsity-promoting crosscorrelation waveform inversion method for high-resolution source imaging. This method imposes sparse constraints on the source PSD in space and inverts the source PSD by minimizing the observed and simulated interstation crosscorrelograms. Compared with the conventional ICCM and LS-ICCM methods, the proposed SP-ICCM method generates source images with much higher resolution and is more robust to random noise present in the data. The increase in the spatial resolution of images in SP-ICCM provides a greater ability to separate multiple sources excited close to each other in space and time. Similar to other seismic imaging techniques, SP-ICCM could be applied to the source localization problem at different scales from engineering to global seismology.

DATA AND MATERIALS AVAILABILITY

Data associated with this research are confidential and cannot be released.

REFERENCES

Aki, K., and P. G. Richards, 2002, Quantitative seismology: University Science Books.

Artman, B., I. Podladtchikov, and B. Witten, 2010, Source location using time-reverse imaging: Geophysical Prospecting, **58**, 861–873, doi: 10.1111/j.1365-2478.2010.00911.x.

Barton, G., 1989, Elements of Green's functions and propagation: Potentials, diffusion, and waves: Oxford University Press.

Basini, P., T. Nissen-Meyer, L. Boschi, E. Casarotti, J. Verbeke, O. Schenk, and D. Giardini, 2013, The influence of nonuniform ambient noise on crustal tomography in Europe: Geochemistry Geophysics Geosystems, **14**, 1471–1492, doi: 10.1002/ggge.20081.

Beck, A., and M. Teboulle, 2009, A fast iterative shrinkage-thresholding algorithm for linear inverse problems: SIAM Journal on Imaging Sciences, **2**, 183–202, doi: 10.1137/080716542.

Bunch, J. R., and L. Kaufman, 1977, Some stable methods for calculating inertia and solving symmetric linear systems: Mathematics of Computation, **31**, 163–163, doi: 10.1090/S0025-5718-1977-0428694-0.
Claerbout, J., 1992, Earth soundings analysis: Processing versus inversion: Blackwell Science.
Cupillard, P., and Y. Capdeville, 2010, On the amplitude of surface waves obtained by noise correlation and the capability to recover the attenuation: A numerical approach: Geophysical Journal International, **181**, 1687–1700, doi: 10.1111/j.1365-246X.2010.04586.x.
Douma, J., R. Snieder, A. Fish, and P. Sava, 2013, Locating a microseismic event using deconvolution: 83th Annual International Meeting, SEG, Expanded Abstracts, 2206–2211, doi: 10.1190/segam2013-0446.1.
Ermert, L., A. Villaseñor, and A. Fichtner, 2016, Cross-correlation imaging of ambient noise sources: Geophysical Journal International, **204**, 347–364, doi: 10.1093/gji/ggv460.
Fichtner, A., 2014, Source and processing effects on noise correlations: Geophysical Journal International, **197**, 1527–1531, doi: 10.1093/gji/ggu093.
Fichtner, A., L. Stehly, L. Ermert, and C. Boehm, 2017, Generalized interferometry — I: Theory for interstation correlations, Geophysical Journal International, **208**, 603–638, doi: 10.1093/gji/ggw420.
Fink, M., 2006, Time-reversal acoustics in complex environments: Geophysics, **71**, no. 4, SI151–SI164, doi: 10.1190/1.2215356.
Gajewski, D., and E. Tessmer, 2005, Reverse modelling for seismic event characterization: Geophysical Journal International, **163**, 276–284, doi: 10.1111/j.1365-246X.2005.02732.x.
Gao, W., M. Sacchi, and Z. Li, 2017, Microseismic-source location via elastic least-squares full-waveform inversion with a group sparsity constraint: 87th Annual International Meeting, SEG, Expanded Abstracts, 2814–2819, doi: 10.1190/segam2017-17785680.1.
Gizon, L., and A.C. Birch, 2002, Time-distance helioseismology: The forward problem for random distributed sources: The Astrophysical Journal, **571**, 966, doi: 10.1086/340015.
Hanasoge, S. M., 2013, The influence of noise sources on cross-correlation amplitudes: Geophysical Journal International, **192**, 295–309, doi: 10.1093/gji/ggs015.
Hanasoge, S. M., 2014, Measurements and kernels for source-structure inversions in noise tomography: Geophysical Journal International, **196**, 971–985, doi: 10.1093/gji/ggt411.
Hanasoge, S. M., A. Birch, L. Gizon, and J. Tromp, 2011, The adjoint method applied to time-distance helioseismology: The Astrophysical Journal, **738**, 100, doi: 10.1088/0004-637X/738/1/100.
Kao, H., and S.-J. Shan, 2004, The source-scanning algorithm: Mapping the distribution of seismic sources in time and space: Geophysical Journal International, **157**, 589–594, doi: 10.1111/j.1365-246X.2004.02276.x.
Li, F., Y. Qin, and W. Song, 2019, Waveform inversion-assisted distributed reverse time migration for microseismic location: IEEE Journal of Selected Topics in Applied Earth Observations and Remote Sensing, **12**, 327–1332, doi: 10.1109/JSTARS.2019.2904206.
Li, L., J. Tan, B. Schwarz, F. Staněk, N. Poiata, P. Shi, L. Diekmann, L. Eisner, and D. Gajewski, 2020, Recent advances and challenges of waveform-based seismic location methods at multiple scales: Reviews of Geophysics, **58**, 1–47, doi: 10.1029/2019RG000667.
Martin, G. S., K. J. Marfurt, and S. Larsen, 2002, Marmousi-2: An update model for the investigation of AVO in structurally complex area: 72nd Annual International Meeting, SEG, Expanded Abstracts, 1979–1982, doi: 10.1190/1.1817083.
Maxwell, S. C., J. Rutledge, R. Jones, and M. Fehler, 2010, Petroleum reservoir characterization using downhole microseismic monitoring: Geophysics, **75**, no. 5, 75A129–75A137, doi: 10.1190/1.3477966.
McMechan, G. A., 1982, Determination of source parameters by wavefield extrapolation: Geophysical Journal International, **71**, 613–628, doi: 10.1111/j.1365-246X.1982.tb02788.x.
Moser, T. J., E Landa, and S. A. Petersen, 1999, Velocity model based diffraction filtering: 69th Annual International Meeting, SEG, Expanded Abstracts, 1979–1982, doi: 10.1190/1.1820713.
Nakata, N., and G. Beroza, 2016, Reverse time migration for microseismic sources using the geometric mean as an imaging condition: Geophysics, **81**, no. 2, KS51–KS60, doi: 10.1190/geo2015-0278.1.
Nishida, K., 2014, Source spectra of seismic hum: Geophysical Journal International, **199**, 416–429, doi: 10.1093/gji/ggu272.
Poletto, F. B., and F. Miranda, 2004, Seismic while drilling: Fundamentals of drill-bit seismic for exploration: Elsevier, **35**.
Pujol, J., 2004, Earthquake location tutorial: Graphical approach and approximate epicentral location techniques: Seismological Research Letters, **75**, 63–74, doi: 10.1785/gssrl.75.1.63.
Rector, J. W., III, and B. Marion, 1991, The use of drill-bit energy as a downhole seismic source: Geophysics, **56**, 628–634, doi: 10.1190/1.1443079.
Rickett, J., and S. Fomel, 1999, A second-order fast marching eikonal solver: Stanford Exploration Project Report, 100, 287–293.
Rickett, J., and P. Sava, 2002, Offset and angle-domain common image-point gathers for shot-profile migration: Geophysics, **67**, 883–889, doi: 10.1190/1.1484531.
Rocha, D., P. Sava, J. Shragge, and B. Witten, 2019, 3D passive wavefield imaging using the energy norm: Geophysics, **84**, no. 2, KS13–KS27, doi: 10.1190/geo2018-0251.1.
Sager, K., L. Ermert, C. Boehm, and A. Fichtner, 2018, Towards full waveform ambient noise inversion: Geophysical Journal International, **212**, no. 1, 566–590.
Sava, P., 2011, Micro-earthquake monitoring with sparsely sampled data: Journal of Petroleum Exploration and Production Technology, **1**, 43–49, doi: 10.1007/s13202-011-0005-7.
Sava, P., and S. Fomel, 2006, Time-shift imaging condition in seismic migration: Geophysics, **71**, no. 6, S209–S217, doi: 10.1190/1.2338824.
Scales, J., A. Gersztenkorn, and S. Treitel, 1988, Fast l_p solution of large, sparse, linear systems: Application to seismic travel time tomography: Journal of Computational Physics, **75**, 314–333, doi: 10.1016/0021-9991(88)90115-5.
Schuster, G. T., J. Yu, J. Sheng, and J. Rickett, 2004, Interferometric/daylight seismic imaging: Geophysical Journal International, **157**, 838–852, doi: 10.1111/j.1365-246X.2004.02251.x.
Shabelansky, A. H., A. E. Malcolm, M. C. Fehler, X. Shang, and W. L. Rodi, 2015, Source-independent full wavefield converted-phase elastic migration velocity analysis: Geophysical Journal International, **200**, 954–968, doi: 10.1093/gji/ggu450.
Shapiro, S., 2015, Fluid-induced micro seismicity: Cambridge University Press.
Sharan, S., R. Wang, and F. J. Herrmann, 2018, Fast sparsity-promoting microseismic source estimation: Geophysical Journal International, **216**, 164–181, doi: 10.1093/gji/ggy415.
Sun, J., Z. Xue, S. Fomel, T. Zhu, and N. Nakata, 2016, Full-waveform inversion of passive seismic data for sources and velocities: 86th Annual International Meeting, SEG, Expanded Abstracts, 1405–1410, doi: 10.1190/segam2016-13959115.1.
Sun, J., T. Zhu, S. Fomel, and W. Song, 2015, Investigating the possibility of locating microseismic sources using distributed sensor networks: 85th Annual International Meeting, SEG, Expanded Abstracts, 2485–2490, doi: 10.1190/segam2015-5888848.1.
Thurber, C. H., and E. R. Engdahl, 2000, Advances in global seismic event location, *in* N. Rabinowitz and C. H. Thurber, eds. Advances in seismic event location: Springer, 3–22.
Tromp, J., Y. Luo, S. Hanasoge, and D. Peter, 2010, Noise cross-correlation sensitivity kernels: Geophysical Journal International, **183**, 791–819, doi: 10.1111/j.1365-246X.2010.04721.x.
van Driel, M., L. Krischer, S. C. Stähler, K. Hosseini, and T. Nissen-Meyer, 2015, Instaseis: Instant global seismograms based on a broadband waveform database: Solid Earth, **6**, 701–717, doi: 10.5194/se-6-701-2015.
Waldhauser, F., and W. L. Ellsworth, 2000, A double-difference earthquake location algorithm: Method and application to the northern Hayward fault, California: Bulletin of the Seismological Society of America, **90**, 1353–1368, doi: 10.1785/0120000006.
Witten, B., and J. Shragge, 2015, Extended wave-equation imaging conditions for passive seismic data: Geophysics, **80**, no. 6, WC61–WC72, doi: 10.1190/geo2015-0046.1.
Witten, B., and J. Shragge, 2017a, Image-domain velocity inversion and event location for microseismic monitoring: Geophysics, **82**, no. 5, KS71–KS83, doi: 10.1190/geo2016-0561.1.
Witten, B., and J. Shragge, 2017b, Microseismic image-domain velocity inversion: Marcellus Shale case study: Geophysics, **82**, no. 6, KS99–KS112, doi: 10.1190/geo2017-0263.1.
Woodard, M. F., 1997, Implications of localized, acoustic absorption for heliotomographic analysis of sunspots: The Astrophysical Journal, **485**, 890–894, doi: 10.1086/304468.
Wu, S., Y. Wang, Y. Zheng, and X. Chang, 2017, Microseismic source locations with deconvolution migration: Geophysical Journal International, **212**, 2088–2115, doi: 10.1093/gji/ggx518.
Wu, Y., and G. A. McMechan, 1996, Elastic full-waveform inversion for earthquake source parameters: Geophysical Journal International, **127**, 61–74, doi: 10.1111/j.1365-246X.1996.tb01535.x.
Yang, J., and H. Zhu, 2019, Locating and monitoring microseismicity, hydraulic fracture and earthquake rupture using elastic time-reversal imaging: Geophysical Journal International, **216**, 726–744, doi: 10.1093/gji/ggy460.
Yin, W., S. Osher, D. Goldfarb, and J. Darbon, 2008, Bregman iterative algorithms for l1-minimization with applications to compressed sensing: SIAM Journal on Imaging Sciences, **1**, 143–168, doi: 10.1137/070703983.
Zhang, H., and C. H. Thurber, 2003, Double-difference tomography: The method and its application to the Hayward Fault, California: Bulletin of the Seismological Society of America, **93**, 1875–1889, doi: 10.1785/0120020190.
Zhu, T., J. Sun, D. Gei, J.M. Carcione, P. Cance, and C. Huang, 2019, Hybrid multiplicative time-reversal imaging reveals the evolution of microseismic events: Theory and field-data tests: Geophysics, **84**, no. 3, KS71–KS83, doi: 10.1190/geo2018-0662.1.

Biographies and photographs of the authors are not available.